

## Research Paper

## Evaluating the effect of slope angle on the distribution of the soil–pile pressure acting on stabilizing piles in sandy slopes



Yi He, Hemanta Hazarika, Noriyuki Yasufuku, Zheng Han \*

Department of Civil and Structural Engineering, Kyushu University, Fukuoka 819-0395, Japan

## ARTICLE INFO

## Article history:

Received 9 September 2014

Received in revised form 9 May 2015

Accepted 11 May 2015

## Keywords:

Stabilizing piles

Sandy slope

Soil arching

Slope angle

Limit equilibrium method

## ABSTRACT

In the past, the response of stabilizing piles subjected to lateral soil movement or lateral force loading has been analysed assuming that the piles are embedded in horizontal semi-infinite soil grounds. In this study, a limit equilibrium method analysing the lateral force (soil–pile pressure per unit thickness) on stabilizing piles embedded in semi-infinite slopes is presented. In addition, the soil arching effects between two neighbouring stabilizing piles are analysed, and the lateral active stress in the rear of the piles is obtained. Furthermore, the squeezing effect between two piles proposed by Ito and Matsui is combined with the lateral active stress in the slope to evaluate the distribution of the soil–pile pressure per unit length of the stabilizing piles in sandy slopes. A numerical simulation using FLAC<sup>3D</sup> is used to evaluate the proposed approach. The simulation shows that the proposed model could reasonably predict the shape of the distribution of the soil–pile pressure acting on the stabilizing piles, while some discrepancy exists between the numerical results and predicted values. Furthermore, the prediction of the proposed model is also evaluated through comparison to the experimental data from the published literature. Parametric analysis is carried out to investigate the influence of the slope angle on the distribution of the soil–pile pressure. The shape of the distribution of the soil–pile pressure acting on the piles is shown to vary with the angle of the slope, while the magnitude of the soil–pile pressure remains in the same order.

© 2015 Elsevier Ltd. All rights reserved.

## 1. Introduction

In the past several decades, installing rows of drilled shafts for slope stabilization has proved to be a reliable and effective technique to prevent excessive slope movement [14,7,19,20,10]. Piles are installed through the unstable soil layer and embedded into the stable layer below the sliding surface. The slope is stabilized by piles, which are able to transfer part of the force from the failing mass to the stable soil layer. For passive piles, the soil–pile pressure applied on the piles by the unstable layer is dependent on the soil movement, which is in turn affected by the presence of the piles [28].

Evaluating soil–pile pressure acting on stabilizing piles is of great significance for the study of slope stabilization. In previous research, a horizontal semi-infinite soil ground was typically used for the theoretical analysis of the soil–pile pressure on piles [14,24,26]. Satisfactory results have been predicted by these methods. In subsequent research [15,16,12,5,29,18,13], these methods

have been adopted and developed. The interaction between piles is governed by the so-called arching effect. Durrani et al. [8] suggested that the Rankine passive and active pressure coefficients should be employed to estimate the maximum spacing resulting in arching between piles. Viggiani [26] suggested designing slope stabilizing piles using the limit equilibrium method. With such an approach, the stabilizing contribution given by a single pile depends on the pile characteristics (diameter, length, and ultimate bending moment), the soil strength and slide thickness [20].

Poulos [24] presented an analysis method in which a simplified form of the boundary element method (Poulos 1973) was employed to study the response of a row of passive piles incorporated in limit equilibrium solutions of slope stability. This method revealed the existence of three modes of failure: (i) “flow mode”, (ii) “short-pile mode”, and (iii) “intermediate mode”. This finding contributed to the practical design of stabilizing piles. Poulos [24] highlighted that the flow mode created the least damage effect of soil movement on the pile; if the piles required protection, efforts should be made to promote this mode of behaviour.

Norris [22] developed a strain wedge (SW) model to predict the response of a flexible pile under lateral loading. Generally speaking, the SW model allows the assessment of the nonlinear  $p$ – $y$

\* Corresponding author at: West 2-1108, Kyushu University, 744 Motoooka, Nishi-ku, Fukuoka 819-0395, Japan. Tel.: +81 092 802 3381; fax: +81 092 802 3378.  
E-mail address: [hankzzz@163.com](mailto:hankzzz@163.com) (Z. Han).

curve response of a laterally loaded pile based on the envisioned relationship between the three-dimensional response of a flexible pile in the soil to its one-dimensional beam on elastic foundation parameters [1]. The SW model has been improved and modified to accommodate a laterally loaded pile embedded in multiple soil layers [1,2]. Undoubtedly, great improvements have been made on the SW model to predict the response of flexible piles under lateral loading [2,3]. In the SW model, the “flow mode” mechanism [24] mentioned previously was adopted in Ashour and Ardlan’s research [4]. Such a slope-pile displacement mechanism is also adopted in the model presented here.

In this paper, the authors propose a simple method for estimating the ultimate soil–pile pressure per unit length of the pile, which is induced by flowing soil, assuming that the soil displacement is larger than the pile deflection (Fig. 1). The theory of plastic deformation [14] is modified, and the soil arching effects between two neighbouring piles are considered, which leads to the nonlinear distribution of the soil–pile pressure per unit length of piles. Furthermore, the theoretical analysis of the effect of the slope angle on the soil–pile pressure distribution in sandy slopes is carried out.

In this study, the soil–pile pressure per unit length of the stabilizing pile is analysed in a semi-infinite sandy slope, as shown in Fig. 2. The general analysis of the soil–pile pressure acting on the piles involves three main steps: (1) analysing the soil arching zone adjacent to the piles in the slope; (2) analysing the active lateral stress in the soil arching zone between two neighbouring piles; and (3) substituting the active lateral stress into Ito and Matsui’s approach [14] to estimate the soil–pile pressure acting on each pile. The piles are assumed to be flexible. In step 1, when the unstable soil layer slides along the potential sliding surface, the soil layer deforms. Additionally, soil arching occurs adjacent to the two neighbouring piles in the failing mass. The plan view of the soil arching zone between two neighbouring piles is shown by the hatched area in Fig. 3(a). A typical cross section  $UU'$  is shown in Fig. 3(b). The area of the soil arching zone is dependent on the slope angle and the properties of the soil, which are discussed later in this paper. In step 2, to simplify the analysis of the active stress on the plane  $AA'$  (referring to Fig. 4), an assumption is made that when the active stress on the plane  $AA'$  is analysed, the area between the parallel lines  $AG$  and  $AG'$  is considered to be the soil arching area. This soil arching area is shown as the shadowed portion in Fig. 4, where  $\sigma_a$  is the active soil stress induced by the soil arching effects,  $D_1$  is the centre-to-centre interval between two neighbouring piles, and  $D_2$  is the clear interval between piles. In addition, the limit equilibrium condition of the differential element

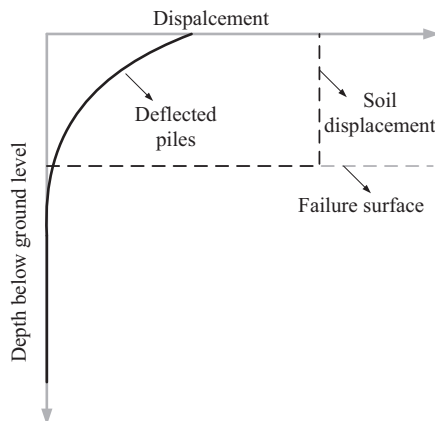


Fig. 1. Soil–pile displacement as employed in the model presented here (Ashour and Ardlan’s research [4]).

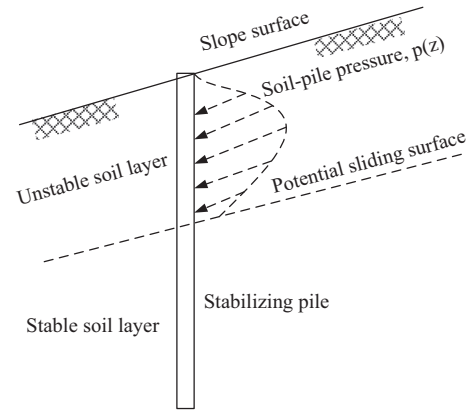


Fig. 2. Stabilizing pile embedded into a semi-infinite slope (adopted from Ashour and Ardlan [4]).

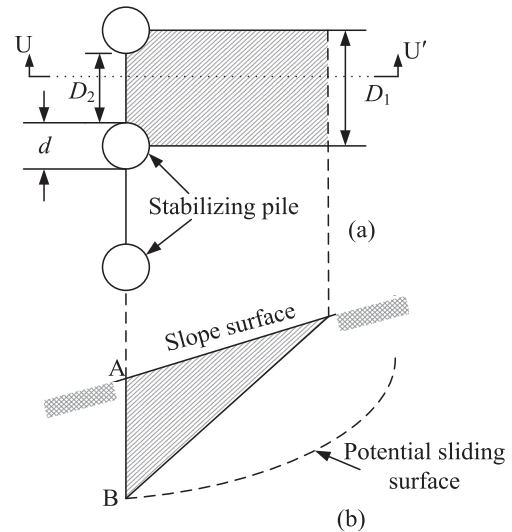


Fig. 3. Soil arching adjacent to the stabilizing piles in a slope: (a) plan view of the soil arching zone; (b) cross section of the soil arching zone in the slope.

in the soil arching zone is analysed to obtain the active stress. In step 3, the approach proposed by Ito and Matsui [14] is adopted, and the squeezing effects between the piles are evaluated. This procedure yields the soil–pile pressure per unit length of the pile.

For the purpose of verifying the proposed model, a numerical simulation was performed. The shear strength reduction method (SRM) is used in the code of  $FLAC^{3D}$ . SRM has been used in the stability analysis of slopes without piles by many previous researchers [30,25,9,28]. This method is extended to analyse the safety factor of a slope stabilized with piles. In the studies by Martin and Chen [21], Won et al. [29], Wei and Cheng [28], and Lirer [20],  $FLAC^{3D}$  is used to analyse the response of the stabilizing piles or the safety factor of the reinforced slope with piles.  $FLAC^{3D}$  is a widely used tool for estimating the response of the stabilizing piles. In this study, the authors use the three-dimensional finite difference code  $FLAC^{3D}$  by SRM to analyse the soil–pile pressure acting on stabilizing piles during slope slides. The numerical simulation results are compared to the prediction obtained from the proposed model. Furthermore, the laboratory experiments carried out by Chen et al. [6] and Guo and Ghee [11] are introduced to evaluate the proposed model.

Finally, the validated model is used to evaluate the effect of slope angle on the distribution of the soil–pile pressure per unit

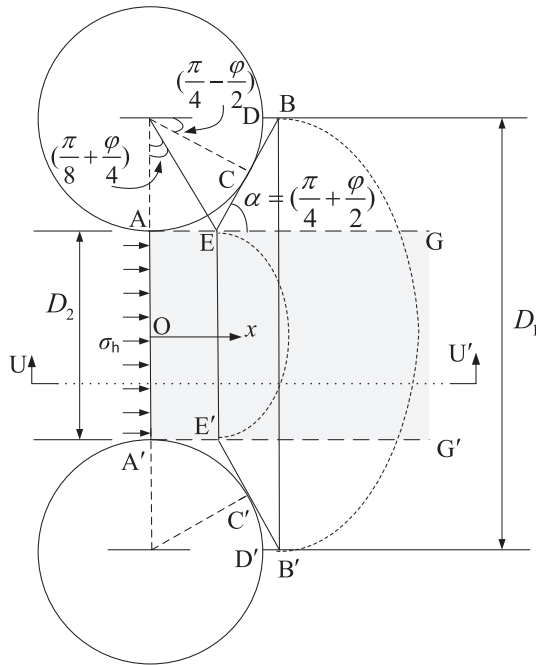


Fig. 4. Plastic deformation of soil between neighbouring piles (adopted from Ito and Matsui [14]).

thickness on the stabilizing piles. The main finding of this paper is that the distribution shape of the soil–pile pressure varies with the slope angle, while the magnitude of the soil–pile pressure remains in the same order.

**2. The soil arching zone**

In a semi-infinite inclined soil mass, the soil arching that occurs adjacent to stabilizing piles has been studied by Wang and Yen [27]. However, the area of the soil arching zone was not specified. Paik and Salgado [23] assumed that the slip plane behind a retaining wall had an angle of  $45^\circ + \varphi/2$  and that the area between the slip plane and the wall was the soil arching zone. In this study, the soil arching zone is analysed using geometry. It is assumed that when the unstable soil layer slides along the potential sliding surface, the soil layer deforms, and a slip plane occurs behind the piles, which is inclined at an angle  $\theta$  with respect to the slope surface (Fig. 5). The area ABC in Fig. 5 is the soil arching zone. The geometry in the soil arching zone is analysed and shown in Appendix A. The angle between the slip plane and the horizontal is expressed as follows:

$$\theta = \frac{1}{2} \left( \varphi - \beta + \arccos \frac{\sin \beta}{\sin \varphi} \right) \tag{1}$$

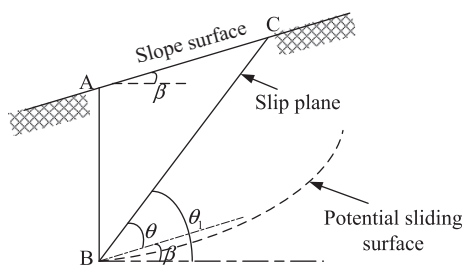


Fig. 5. Profile of the soil arching zone and the geometric relationships in the zone.

$$\theta_1 = \frac{1}{2} \left( \varphi + \beta + \arccos \frac{\sin \beta}{\sin \varphi} \right) \tag{2}$$

where  $\varphi$  is the internal friction angle of the soil,  $\beta$  is the inclined angle of the slope surface, and  $\theta_1$  is the angle between the slip plane and the horizontal.

**3. Theoretical analysis**

**3.1. Rotation of the major and minor stresses in the soil arching zone**

In the study of retaining walls, soil arching is assumed to occur in a circular arc. Paik and Salgado [23] have evaluated the active soil stress based on the soil arching theory. In this paper, the approach proposed by Paik and Salgado [23] is adopted and extended to analyse an inclined soil mass. The rotation of the principal stress on the line AB (Fig. 5) is described in Fig. 6(a) and (b). In the rear of line AB, the trajectory of the minor principal stress on the differential element is represented by dotted lines assumed as an arc, while the major principal stress is the normal to the arc. The active earth pressure acting on line AB includes two components: the active lateral stress  $\sigma_h$  and the shear stress  $\tau$ .

As shown in Fig. 6(a), on the left side of the differential element, the force equilibrium in the triangular element at point E is considered. The lateral stress is calculated as follows:

$$\sigma_h = \sigma_1 \cos^2 \theta + \sigma_3 \sin^2 \theta \tag{3}$$

Similarly, at an arbitrary point D on the arc, whose original location is point F, the lateral force is given by

$$\sigma_{ah} = \sigma_1 \cos^2 \psi + \sigma_3 \sin^2 \psi \tag{4}$$

where  $\psi$  is the angle between the normal of the arc at point D and the horizontal, and  $\sigma_{ah}$  is the lateral stress at point D. Considering when the soil is in an active condition, substituting  $\sigma_3/\sigma_1 = 1/N$  into Eq. (4) yields

$$\sigma_{ah} = \left( \cos^2 \psi + \frac{1}{N} \sin^2 \psi \right) \sigma_1 \tag{5}$$

where  $N = \tan^2(45^\circ + \varphi/2)$ .

In Fig. 7(a), the vertical stress  $\sigma_v$ , which is applied on the surface of the differential element, includes two components: one perpendicular to the line EP,  $\sigma'_v$ , and one parallel to the line EP,  $\sigma_f$ . The ratio of  $\sigma_v$  to  $\sigma'_v$  is as follows:

$$\sigma_v/\sigma'_v = \frac{1}{\cos \beta} \tag{6}$$

Because  $\sigma_{ah} - \sigma_3 = \sigma_1 - \sigma_v$ , substituting for  $\sigma_{ah}$  yields

$$\frac{\sigma'_v}{\sigma_1} = \cos \beta \left( \sin^2 \psi + \frac{1}{N} \cos^2 \psi \right) \tag{7}$$

Because the angle  $\psi$  (Fig. 6(a)) is not a constant, an average stress  $\bar{\sigma}'_v$  is introduced to replace  $\sigma'_v$  at every point. This average stress is given by

$$\bar{\sigma}'_v = \frac{V'}{S} \tag{8}$$

where  $V'$  is a component of the total stress applied on the differential element, which is perpendicular to EP, and  $S$  is the width of the differential element (referring to Fig. 6(b)). Considering the geometry depicted in Fig. 6(b),  $S$  is calculated by

$$S = \frac{\cos(\theta_w + \xi)}{\cos(\beta + \xi)} R \tag{9}$$

where  $\xi$  is the angle between the normal line OQ and the vertical and  $R$  is the radius of the circle.

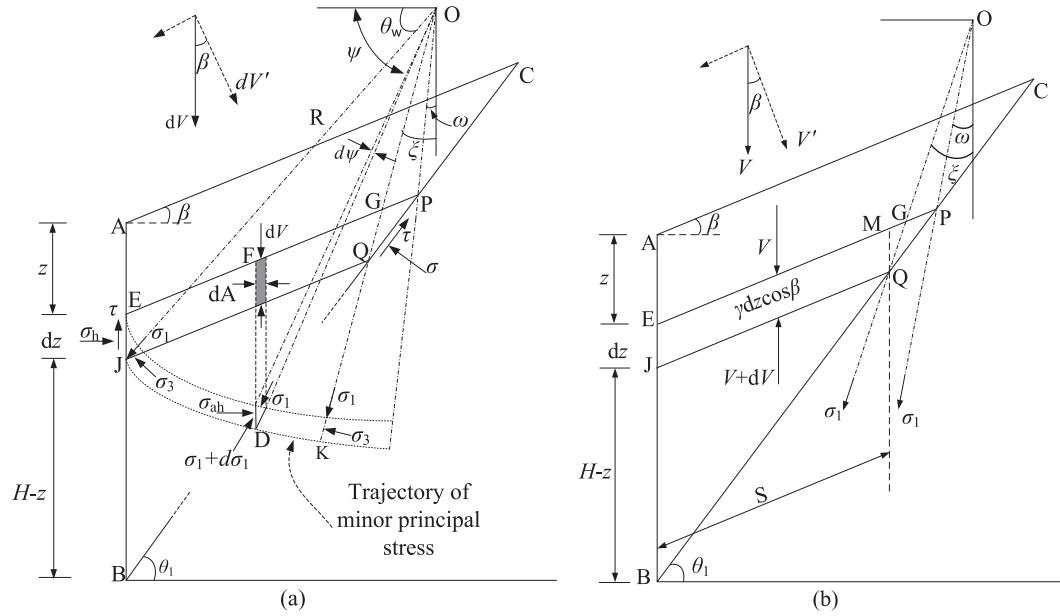


Fig. 6. Stress on the differential element in the soil arching zone: (a) the major and minor principal stresses; (b) schematic of the vertical total force on the differential element (based on [23]).

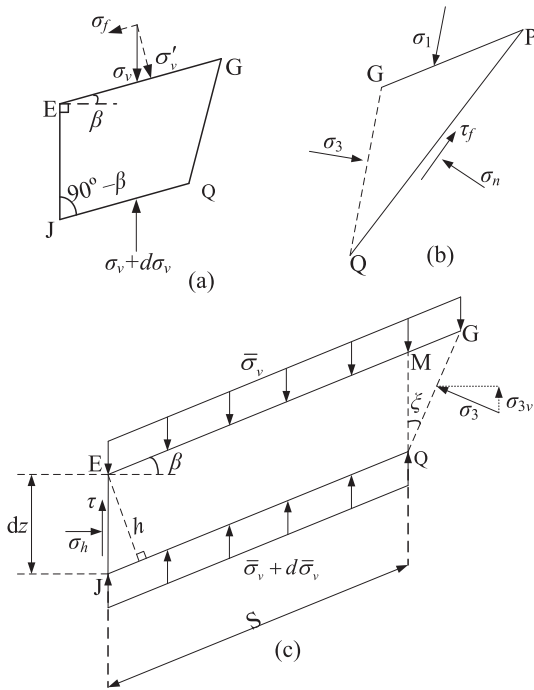


Fig. 7. Stress on the differential element: (a) major and minor principal stresses applied on the right edge of the differential element; (b) two components of the vertical stress on the differential element; (c) stress on the main part of the differential element.

The stress  $V'$  on the differential element can be calculated by

$$V' = \int_{\theta_w}^{\pi/2-\omega} dV' \quad (10)$$

where  $dV'$  is the differential force on the shaded element at point F, which is perpendicular to EP (referring to Fig. 6(a)). This perpendicular differential force is expressed as

$$dV' = \sigma'_v dA = \sigma_1 \cos \beta \left( \sin^2 \psi + \frac{1}{N} \cos^2 \psi \right) \cdot \frac{Rd\psi \sin \psi}{\cos \beta} \quad (11)$$

Solving Eq. (8)–(11) yields

$$\bar{\sigma}'_v = \frac{\cos(\beta + \xi)}{\cos(\theta_w + \xi)} \cos \theta_w \left( 1 - \frac{N-1}{3N} \cos^2 \theta_w \right) \sigma_1 \quad (12)$$

To simplify the analysis process, the angle  $\omega$  (referring to Fig. 6) is assumed to be 0.

Comparing this result to Eq. (6), it is reasonable to express the average vertical stress on the differential element as

$$\bar{\sigma}_v = \frac{1}{\cos \beta} \bar{\sigma}'_v \quad (13)$$

Substituting Eq. (12) into Eq. (13) yields

$$\bar{\sigma}_v = \frac{\cos(\beta + \xi)}{\cos(\theta_w + \xi) \cos \beta} \cos \theta_w \left( 1 - \frac{N-1}{3N} \cos^2 \theta_w \right) \sigma_1 \quad (14)$$

Using Eqs. (3) and (14), a ratio  $K_{an}$  of the active lateral stress acting on the plane AB to the average vertical stress over the differential element is derived:

$$K_{an} = \frac{\sigma_h}{\bar{\sigma}_v} = \frac{\cos(\theta_w + \xi) \cos \beta}{\cos(\beta + \xi) \cos \theta_w} \cdot \frac{3(N \cos^2 \theta_w + \sin^2 \theta_w)}{3N - (N-1) \cos^2 \theta_w} \quad (15)$$

### 3.2. The limit equilibrium equation on the differential element

To evaluate the lateral stress on the line AB (Fig. 6(a)), a detailed analysis of the differential element is required. On the right edge of the differential element (Fig. 6(a)), because the direction of the major principal stress is along the line OG, the major and minor principal stresses are considered to be applied on surfaces GP and GQ, respectively, of the triangular differential element GPQ, which is shown in Fig. 7(b). In Fig. 7(b), the triangular element GPQ is shown in an equilibrium state, which allows this triangular element to be ignored when analysing the vertical stress for the entire differential element. In Fig. 7(c), the minor principal stress  $\sigma_3$  is loaded on the line GQ,  $\sigma_{3v}$ , which is the vertical component of  $\sigma_3$  and is expressed as

$$\sigma_{3v} = \sigma_3 \sin \xi \frac{\cos \beta}{\cos(\xi + \beta)} \quad (16)$$

where  $\xi$  is the angle between the normal line OQ and the vertical. Based on the geometry between the slip surface and the major principal plane,  $\xi$  is calculated by

$$\xi = \frac{\pi}{4} + \frac{\varphi}{2} - \theta_1 = \frac{1}{2} \left( \frac{\pi}{2} - \beta - \cos^{-1} \frac{\sin \beta}{\sin \varphi} \right) \quad (17)$$

In addition, on the left edge of the differential element, the shear stress is

$$\tau = \sigma_h \tan \varphi = \bar{\sigma}_v K_{an} \tan \varphi \quad (18)$$

Ignoring the stress loaded on the segment MG and considering the clear interval between the two neighbouring piles, the summation of all vertical forces acting on the main part of the differential element (Fig. 7(c)) gives

$$d\bar{\sigma}_v \cdot SD_2 + \bar{\sigma}_v K_{an} \tan \varphi \cdot D_2 dz - \bar{\sigma}_v K_{an} \tan \beta \cdot D_2 dz + \sigma_3 \sin \xi \frac{\cos \beta}{\cos(\xi + \beta)} dz \cdot D_2 = \gamma S \cdot h D_2 \quad (19)$$

Using  $\sigma_3 = \sigma_1/N$ , Eqs. (13) and (14), the minor principal stress is

$$\sigma_3 = \frac{K_{an}}{N \cos^2 \theta_w + \sin^2 \theta_w} \bar{\sigma}_v \quad (20)$$

Substituting Eq. (20) into Eq. (19) and considering that  $S = (H - z) \cos \theta_1 / \sin \theta$ ,  $h = \cos \beta \cdot dz$ , Eq. (19) is solved as

$$\bar{\sigma}_v = \frac{\gamma H \cos \beta}{1 - (K_{an} \tan \varphi - K_{an} \tan \beta + m) \frac{\sin \theta}{\cos \theta_1}} \times \left[ \left( 1 - \frac{z}{H} \right)^{(K_{an} \tan \varphi - K_{an} \tan \beta + m) \frac{\sin \theta}{\cos \theta_1}} - \left( 1 - \frac{z}{H} \right) \right] \quad (21)$$

where  $m$  is a function of  $\beta$ , given by

$$m = \frac{K_{an} \sin \xi \cos \beta}{(N \cos^2 \theta_w + \sin^2 \theta_w) \cos(\xi + \beta)} \quad (22)$$

where  $\theta_w = \pi/4 + \varphi/2$ . Multiplying Eq. (21) by  $K_{an}$ , the lateral soil stress on the line AB (Fig. 6(a)) is estimated by

$$\sigma_h = \frac{K_{an} \gamma H \cos \beta}{1 - (K_{an} \tan \varphi - K_{an} \tan \beta + m) \frac{\sin \theta}{\cos \theta_1}} \times \left[ \left( 1 - \frac{z}{H} \right)^{(K_{an} \tan \varphi - K_{an} \tan \beta + m) \frac{\sin \theta}{\cos \theta_1}} - \left( 1 - \frac{z}{H} \right) \right] \quad (23)$$

Note that as mentioned previously, the analyses of the active earth pressure  $\sigma_h$  are based on Paik and Salgado's outstanding work [23], so that Eqs. (3)–(5) are similar to their research. However, the incline of the soil mass is considered in this paper, which leads to different boundary conditions and different expressions of the earth pressure  $\sigma_h$ . Moreover, if  $\beta = 0$ , Eq. (23) simplifies to be the same as the equation proposed by Paik and Salgado [23]. This reveals that the equation in Paik and Salgado's research [23] is the special case of this proposed model.

### 3.3. The squeezing effects between two neighbouring piles

Ito and Matsui [14] have proposed a plastic deformation model to evaluate the squeezing effects between two neighbouring piles. In this paper, a similar concept is used; all of the assumptions for the soils implied by Ito and Matsui [14] are also adopted. The soil–pile pressure per unit length of the stabilizing piles in sandy slopes is expressed as

$$p = \frac{\gamma H K_{an} \cos \beta}{1 - (K_{an} \tan \varphi - K_{an} \tan \beta + m) \frac{\sin \theta}{\cos \theta_1}} \times \left[ \left( 1 - \frac{z}{H} \right)^{(K_{an} \tan \varphi - K_{an} \tan \beta + m) \frac{\sin \theta}{\cos \theta_1}} - \left( 1 - \frac{z}{H} \right) \right] \times \left\{ D_1 \left( \frac{D_1}{D_2} \right)^{N^{1/2} \tan \varphi + N - 1} \times \exp \left[ \frac{D_1 - D_2}{D_2} N \tan \varphi \tan \left( \frac{\pi}{8} + \frac{\varphi}{4} \right) \right] - D_2 \right\} \quad (24)$$

The details of the derivation of Eq. (24) are given in the appendix. In addition, the details of the formulae used to calculate the total lateral force on a pile and the point application of the force are also included in the appendix.

## 4. Numerical evaluation

A numerical model of the stabilized slope with piles was constructed in the numerical finite difference program FLAC<sup>3D</sup>. Additionally, SRM was used to analyse the soil–pile pressure on the piles when the slope failed. In the numerical model, the piles were formatted by the intrinsic structure element. The slope model is shown in Fig. 8 with a vertical to horizontal gradient of 1:3. Three piles with a length of 9 m were installed in a row in the middle of the slope. The interval between two neighbouring piles was  $D_1 = 3$  m and  $D_2 = 2.6$  m. The width of the model was 9 m. At the bottom boundary of the model mesh, zero displacement was imposed. Stress boundary conditions were imposed at both the

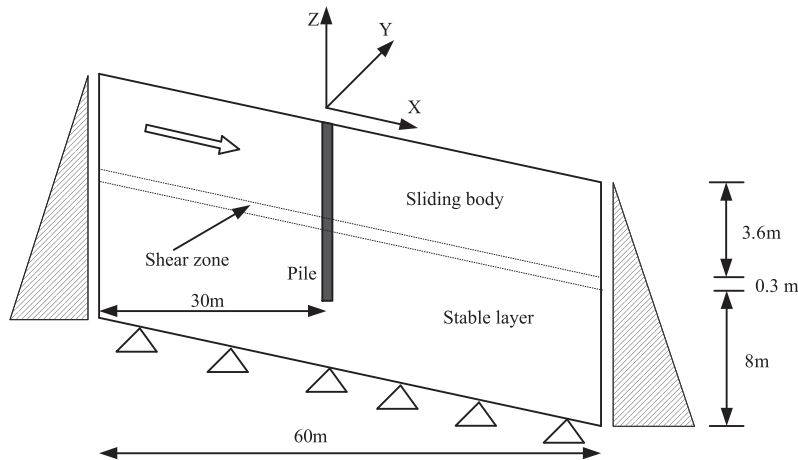


Fig. 8. Slope model used in FLAC<sup>3D</sup>.

**Table 1**  
Material properties adopted in the numerical model.

	Sliding body	Shear zone	Stable layer	Pile
$\gamma$ (kN/m <sup>3</sup> )	19	19	20	25
$E$ (Pa)	3.8e7	2e7	7.8e7	3e10
$\mu$	0.32	0.32	0.32	0.2
$c$ (kPa)	0	0	100	–
$\varphi$ (°)	32	30	30	–
$\psi$ (°)	0/2	0	0	0

uphill and downhill truncation planes. The soil was modelled using the Mohr–Coulomb model, and the material properties are shown in Table 1.

The model was first brought to equilibrium under gravity loading. Next, a gradual reduction of the shear strength was imposed along the shear zone. To simulate the existence of an accumulation zone, the SRM was not imposed on the downslope final stretch of the shear zone for a length of 10 m. This method of simulating the resistance of the accumulation zone was proposed by Lirer [20]. Incorporating the soil properties, pile geometries and the height of the sliding soil above the shear zone, the soil–pile pressure acting on the piles was calculated by Eq. (24), and the results are shown in Fig. 9(a). For comparison, a prediction using Ito and

Matsui’s approach [14] and the results from FLAC<sup>3D</sup> are included in Fig. 9(a) as well.

A well-instrumented field trial was carried out by Lirer [20] to study the influence of the row of piles on the local and overall mudslide displacement field, as well as to quantify the shear forces and bending moments within the piles. The experimental findings have been back analysed by numerical simulation [20]. In this study, in addition to the numerical model mentioned above, both the observed data of the field trial and the numerical result obtained by Lirer [20] were used to validate the proposed approach. The material properties used in Lirer’s model are shown in Table 2. The section of Lirer’s model was similar to Fig. 8, replacing the dimensions with 300 m in length, 25 m in height, and 8 m in width. In addition, the slope angle was 11° in Lirer’s research. For more details of the field experiment and Lirer’s numerical model, see the source reference. The comparison is shown in Fig. 9(b).

Fig. 9(a) shows the comparison between the numerical simulation results and the prediction of two theoretical methods with a slope angle of 18.4°. Fig. 9(b) shows the observed data, the numerical results and the theoretical methods estimations with a slope angle of 11°. Both figures reveal that the distribution of the soil–pile pressure computed by the proposed model is nonlinear, while the prediction from Ito and Matsui’s approach appears to be linear; however, the orders of magnitude of the two theoretical methods’ results are in line with each other. In Fig. 9(b), the observed data shows that in the upper part of the sliding soil, within approximately 1 m depth, the soil–pile pressure is negative. Such a distribution of the soil–pile pressure on top of the pile is thought to have been obtained as a result of influences of the pile deformation and the non-uniform movements of the sliding soils. However, the prediction of the soil–pile pressure on the top of the pile is positive because the flow mode [24] is considered in this proposed model, where the soil displacement is assumed to be larger than the pile deflection and the soil movement is uniform. Ignoring the negative force on the top of the piles, the distribution of the soil–pile pressure on the piles predicted by the proposed approach shows the same trends as the numerical results and the observed data. Particularly in the lower part of the sliding soil, the numerical results and the prediction of the proposed method show that the soil–pile pressure decreases after the first increase, while Ito and Matsui’s approach shows linear increases of the soil–pile pressure. Fig. 9 reveals that the shape of the distribution of the soil–pile pressure estimated by the proposed model is similar to that of the numerical and observed results, while the values are overestimated. For instance, in Fig. 9(a), the maximum value provided by the numerical analysis is 3.64 t/m ( $z = 3.6$  m), compared to 6.39 t/m ( $z = 3.5$  m) and 7.6 t/m ( $z = 4$  m) predicted by the proposed model and Ito and Matsui’s approach, respectively. In addition, the order of magnitude of the predicted values agrees with that of the numerical and observed results. As presented in Fig. 9, the proposed model allows the assessment of the soil–pile pressure based on soil and pile properties assuming that the soil movement is larger than the pile deflection. However, the limited accuracy of the prediction implies that the proposed model needs to be improved in the future.

**Table 2**  
Material properties adopted in Lirer’s model.

	Sliding body	Shear zone	Stable layer	Pile
$\gamma$ (kN/m <sup>3</sup> )	19	19	19	–
$E$ (Pa)	2e7	1e7	5e7	2e11
$\mu$	0.34	0.34	0.34	0.25
$c$ (kPa)	0	0	1000	14e4
$\varphi$ (°)	28	25	30	–
$\psi$ (°)	0	0	0	0

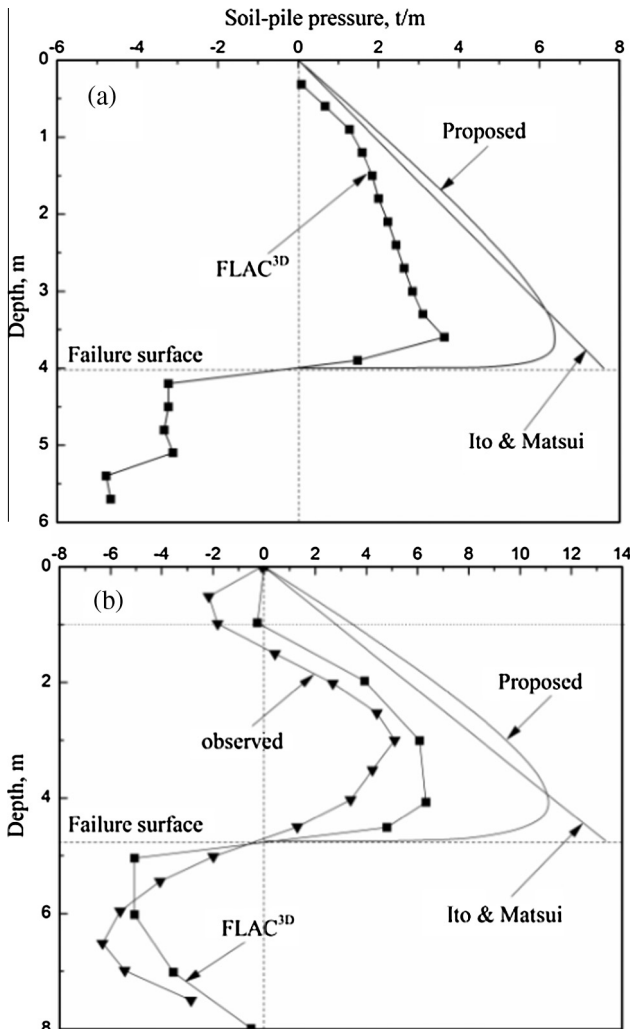


**Fig. 9.** Comparison between the numerical results and predictions: (a) slope angle of 18.4°; (b) slope angle of 11°.

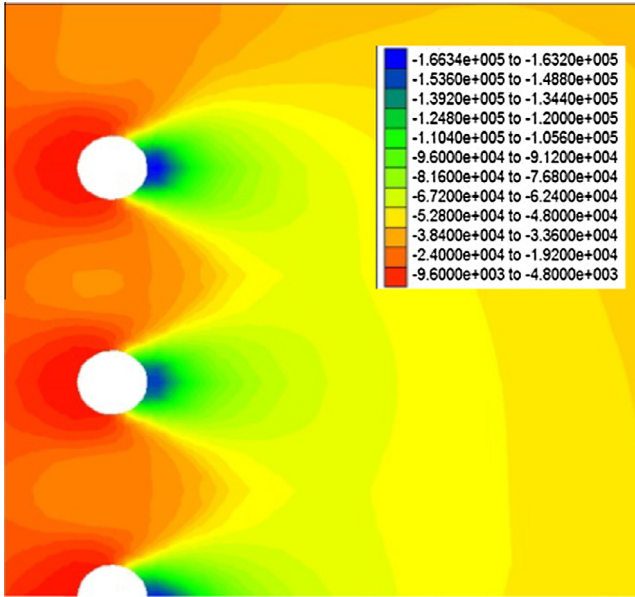


Fig. 10. The stress contours ( $\sigma_{xx}$ ) around the piles.

A simulation with the piles formatted by a number of zones is carried out. The piles with a diameter of 0.6 m and a centre-to-centre interval of 2 m were installed in the slope. The stress contour around the stabilizing piles is plotted in Fig. 10. The passive soil wedge behind each pile and the arching zone between neighbouring wedges are apparent. The shape of the soil arching zone in the stress contours from the plane view appears to be sector. However, as mentioned previously, the soil arching zone in the plane is assumed to be a rectangle for the purpose of simplifying the analysis of the active stress.

### 5. Published experimental studies

Chen et al. [6] have reported on the model tests of pile groups subjected to lateral soil movement. The experimental setup is briefly described below and more details can be found in Polous [24]. The main part of the apparatus consisted of a testing vessel made from a steel sheet and having internal dimensions of 450 mm wide by 565 mm long and 700 mm high. Two vertical steel plates, consisting of two parts hinged at mid-height, were placed across the width inside the box. With a loading system attached to the steel vessel, the upper part of each steel plate could be rotated simultaneously around its hinge and consequently cause the upper part of the sand to move [6]. The model piles were made from aluminium tubes and were 1 m in length and 25 mm in diameter with a 1.2 mm wall thickness. On the instrumented piles, ten full bridge circuit strain gauges were placed at 100 mm intervals inside each pile for measuring the bending moments in the pile. Based on the measured bending moments  $M(z)$ , the shear forces  $T(z)$  and the soil–pile pressure per unit thickness  $p(z)$  can be computed by successive derivations as follows:

$$T(z) = \frac{dM(z)}{dz} \quad (25)$$

$$p(z) = \frac{d^2M(z)}{d^2z} \quad (26)$$

The dry sand used in the model test was calcareous sand taken from Bass Strait, Australia [6]. The piles were installed into the sand bed in a row. The properties of the sand and the pile spacing

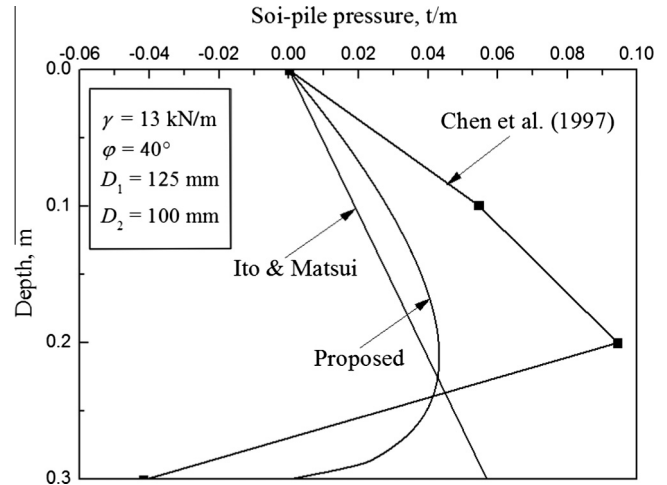


Fig. 11. Comparison of the prediction and the experimental values based on the research of Chen et al. [6].

are shown in Fig. 11. The soil–pile pressure per unit length of the pile is calculated based on Eq. (26), which implies that the depth of the real failure surface around the piles is approximately 0.3 m. The comparison of the predicted and the experimental values is shown in Fig. 11.

In Fig. 11, the prediction using the proposed approach shows a similar trend of soil–pile pressure distribution as the experimental data. The maximum soil–pile pressure obtained by the experiment is 0.094 t/m at a depth of 0.2 m. Meanwhile, the calculated maximum soil–pile pressure is at the same depth and is 0.043 t/m. Fig. 11 shows that the maximum value from the experiment is approximately two times larger than that of the prediction. The sand in the test was subjected to a triangular profile of horizontal movement with depth, while the proposed model is based on a mode of the uniform soil movement. However, compared to Ito and Matsui’s approach, the proposed model provides a relatively similar distribution shape of the soil–pile pressure as the experimental data, although some value discrepancy does exist.

Guo and Ghee [11] conducted the experiment on group effects of piles due to lateral soil movement. The apparatus consisted of a shear box and a loading system that allow different soil movement profiles and vertical loading to be applied simultaneously. The experimental setup is briefly introduced here.

The shear box has internal dimensions of 1 m by 1 m and is 0.8 m in height. The upper moveable part of the box consisted of the desired number of 25 mm thick square laminar aluminium frames to achieve a thickness of  $L_m$  (<400 mm). They were moved together by a rectangular loading block to generate uniform lateral soil movement. The lower fixed section of the box was a timber box 400 mm in height with a number of laminar aluminium frames to achieve a stable sand layer of thickness  $L_s$  ( $\geq 400$  mm). For details of the apparatus and tests, see the source reference.

The sand used in the test was an oven-dried medium-grained quartz, Queensland sand. The model piles used in the tests were made of aluminium tube, 1200 mm in length and 32 mm in outer diameter with a 1.5 mm wall thickness [11]. Two piles were installed into the fixed timber box. The centre-to-centre “joining” line of the piles was perpendicular to the direction of the soil movement. The properties of the sand and the pile spacing are shown in Fig. 12.

Fig. 12 compares the predicted and the experimental values. Above the failure surface, the soil–pile pressure per unit length of the pile predicted by the proposed approach shows the same distribution as the experimental values. In the upper half of the

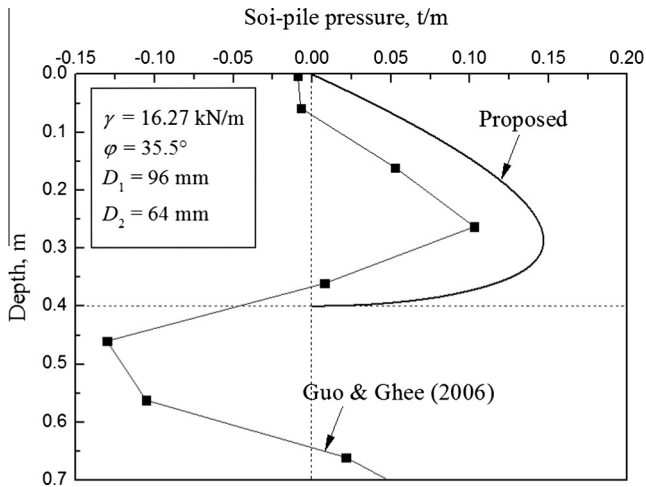


Fig. 12. Comparison of the prediction and the experimental values based on the research of Guo and Ghee [11].

moveable soil, the predicted soil–pile pressure increases linearly until the increment slows down at the depth of 0.2–0.3 m. The maximum soil–pile pressure obtained by the experiment is approximately 0.103 t/m at a depth of 0.26 m, while the predicted maximum value is 0.147 t/m at 0.28 m. Fig. 12 indicates that the order of magnitudes of the soil–pile pressure from the prediction and the experiment are in line with each other.

6. Parametric study

A parametric analysis is implemented based on the proposed analytical model to investigate the influence of the slope angle and the internal friction angle on the distribution of the soil–pile pressure per unit length of the piles. Because the proposed model aims to predict the distribution of the soil–pile pressure on stabilizing piles embedded in a semi-infinite slope, which differs from the models designed for horizontal soil grounds, the angle of the semi-infinite slope is considered to be one of the governing factors. In addition, because the internal friction angle of soils is a primary mechanical property, its effect on the soil–pile pressure distribution of the piles also needs to be analysed.

In the following discussion, the soil–pile pressure distribution, the soil–pile pressure on different pile depths, the total lateral force and the point application of the force with respect to different slope angles and different internal friction angles are analysed. Additionally, for comparison, the corresponding values from Ito and Matsui’s approach are also calculated.

6.1. The influence of slope angle  $\beta$

Fig. 13 shows the distribution of the soil–pile pressure along the stabilizing piles when the sliding soil layer is 4 m thick. The soil properties and geometric parameters are also shown in Fig. 13. The soil–pile pressure on the pile has a nonlinear distribution at every slope angle  $\beta$ . Additionally, with a slope angle  $\beta$  varying from  $0^\circ$  to  $30^\circ$ , the order of magnitude of the soil–pile pressure does not change. The maximum soil–pile pressure and the height of the centroid of the soil–pile pressure increases while the slope angle  $\beta$  increases from  $0^\circ$  to  $25^\circ$ . However, when  $\beta$  varies from  $25^\circ$  to  $30^\circ$ , the maximum soil–pile pressure decreases. Furthermore, Fig. 13 implies that if the magnitude of the soil–pile pressure on a pile is the only factor considered, ignoring the change of the point application of the force with slope angle, it is reasonable to use a

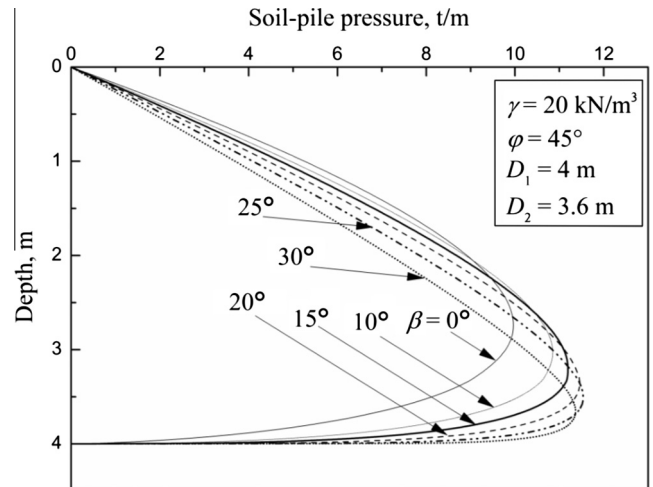


Fig. 13. Distribution of the soil–pile pressure along the piles with respect to different slope angles.

horizontal soil model ( $\beta = 0^\circ$ ) as a simplified way to estimate the response of stabilizing piles in slopes ( $\beta \neq 0^\circ$ ).

Fig. 14 shows the soil–pile pressure at different pile depths with respect to different internal friction angles. The calculated soil–pile

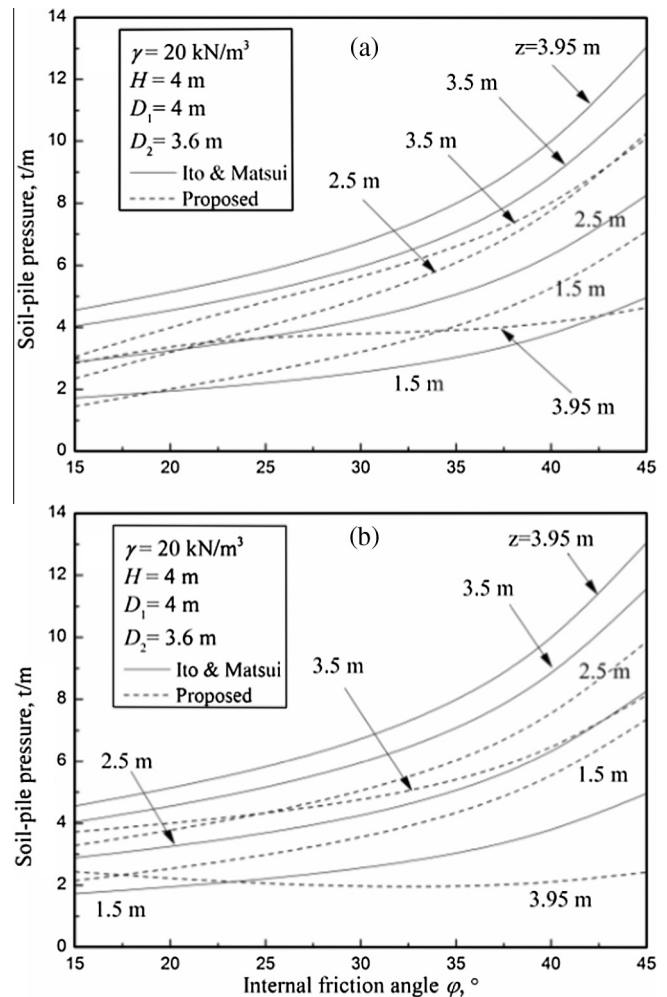


Fig. 14. Soil–pile pressure at different depths of the pile with respect to different internal friction angles: (a)  $\beta = 10^\circ$ ; (b)  $\beta = 0^\circ$ .

pressure denoted by the solid line remains the same while the slope angle varies from 10° to 0°. Moreover, the soil–pile pressures at different depths are almost parallel to each other, which is consistent with the linear distribution of the soil–pile pressure on a pile above the failure surface based on Ito and Matsui’s approach. Conversely, the dotted lines intersect with each other, which reveals the nonlinear distribution of the soil–pile pressure along the pile. For instance, in Fig. 14(b), when the depth  $z$  is equal to 1.5 m and 2.5 m, the soil–pile pressures are nearly parallel to each other, which indicates that on the top of the pile, the soil–pile pressure increases linearly. However, when  $z$  is 3.95 m (close to the failure surface), the soil–pile pressure is less than that at  $z = 2.5$  m and 3.5 m, which indicates a sharp decrease near the failure surface.

In Fig. 13, the area enclosed by the nonlinear distribution of the soil–pile pressure and the vertical coordinate axis represents the total force acting on the pile, which can be obtained by Eq. (A.20). The prediction of the total force as the slope changes is shown in Fig. 15. According to the proposed model, the total force decreases after the first increase when the slope angle varies from 0° to 30°. As the slope angle increases, the total force increases because of the increase of the component of the gravity along the direction of sliding. However, when the slope angle is approximately equal to the internal friction angle, the total force decreases because of the decrease in slope stability.

The height of the resultant lateral force versus the slope angle is displayed in Fig. 16. The height of the resultant lateral force predicted by Ito and Matsui’s approach remains constant at 0.33H, even if the slope angle varies from 0° to 30°. However, the height of the resultant lateral force is a function of the slope angle and the internal friction angle based on the proposed model (Eq. (A.22)). For instance, when  $\varphi = 45^\circ$ , the height of the resultant lateral force varies from 0.423H to 0.351H when the slope angle changes from 0° to 30°. The height of the resultant lateral force appears to be affected by the soil arching that occurs between two neighbouring piles.

6.2. The influence of the internal friction angle  $\varphi$

The soil–pile pressure acting on a pile with respect to different internal friction angles is shown in Fig. 15, and the soil properties and geometric parameters are shown in Fig. 17. The distribution shapes of the soil–pile pressure are similar to each other when the internal friction angle varies from 25° to 40°. Additionally, the maximum soil–pile pressure appears in the range of 0.7H

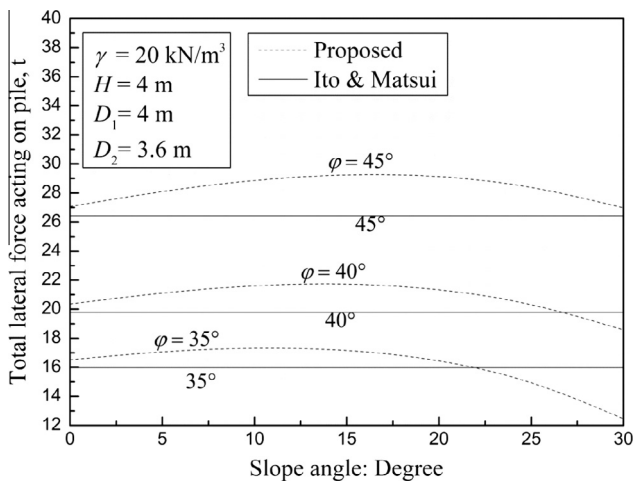


Fig. 15. Effect of the slope angle on the total force on a pile.

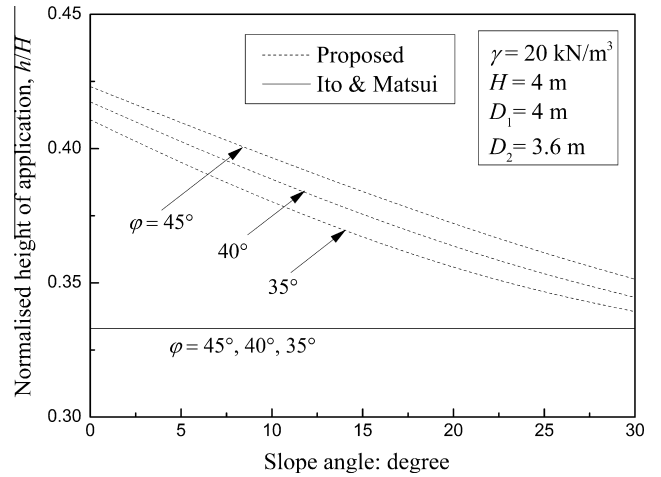


Fig. 16. Change in the height of the resultant lateral force.

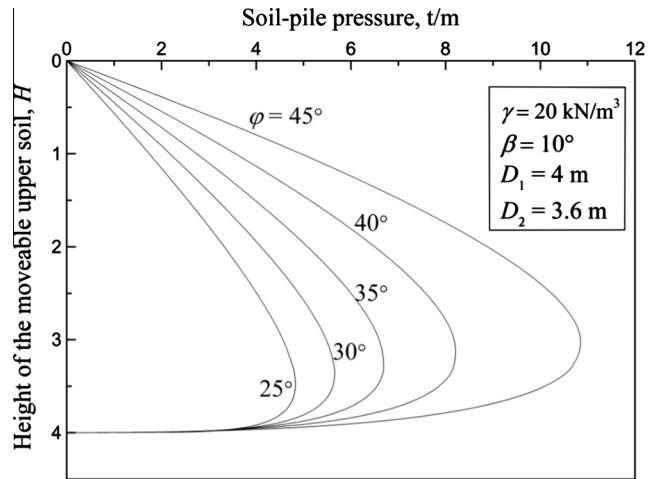


Fig. 17. Effect of the internal friction angle on the soil–pile pressure acting on a pile.

(2.8 m) to 0.9H (3.6 m). The maximum soil–pile pressure for  $\varphi = 40^\circ$  is nearly twice as large as that for  $\varphi = 25^\circ$ . Additionally, the soil–pile pressure on the pile increases when the internal friction angle increases. Compared to Fig. 13, Fig. 17 shows that the internal friction angle has a greater effect on the magnitude of the soil–pile pressure on the pile than the slope angle does.

Fig. 18 displays the effect of the internal friction angle on the total force on the pile. The trends of the total force on the pile from both Ito and Matsui’s approach and the proposed model are similar: when the internal friction angle increases, the total force increases. Additionally, when  $\varphi = 24^\circ$ , the dotted line reveals that the closer that the slope angle approximates the internal friction angle, the smaller the total force estimates. Furthermore, when  $\varphi$  is much larger than  $\beta$ , such as when  $\varphi = 44^\circ$ , the total force appears to approach to the same value among the three different slope angles.

Fig. 19 shows the effect of the internal friction angle on the height of the resultant lateral force. The height of the resultant lateral force remains constant (0.33H) according to Ito and Matsui’s approach. However, based on the proposed model, for instance when  $\beta = 10^\circ$ , the height of the resultant lateral force varies from 0.375H to 0.395H as the internal friction angle increases from 24° to 44°. This difference occurs because in Ito and Matsui’s approach, Rankine theory is used to estimate the lateral active stress, which leads to the constant height of the resultant lateral

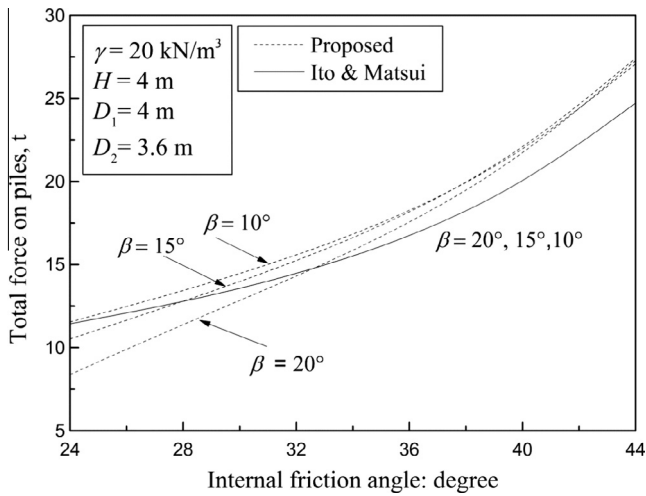


Fig. 18. Effect of the internal friction angle on the total force on a pile.

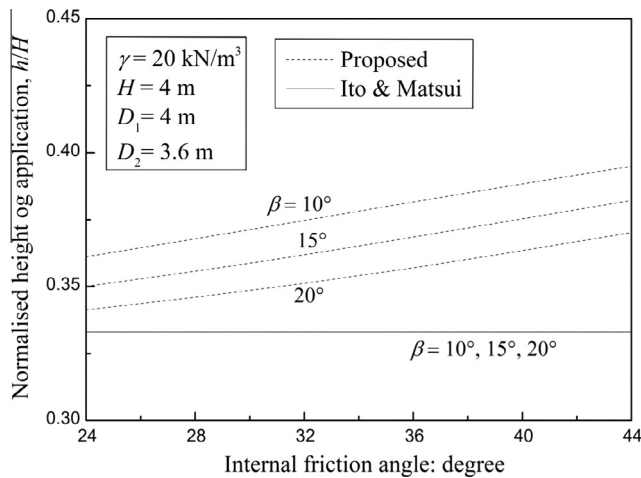


Fig. 19. Effect of the internal friction angle on the height of the resultant lateral force.

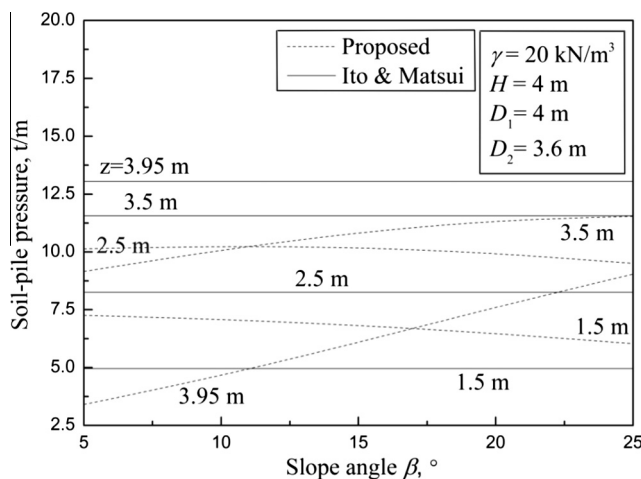


Fig. 20. Soil-pile pressure at different pile depths with respect to different slope angles.

force. Conversely, when the effects of soil arching are considered, the proposed model displays a height that changes with respect to different internal friction angles.

Fig. 20 displays the soil-pile pressure at different pile depths with respect to different slope angles. The internal friction angle  $\varphi$  is  $45^\circ$ . Fig. 20 shows the same trends of the distribution of the soil-pile pressure as Fig. 14. Moreover, along the upper half of the pile, the soil-pile pressures calculated by Ito and Matsui's approach are always less than that calculated using the proposed method. Along the lower half of the pile, changeover of the soil-pile pressure occurs.

### 7. Discussion

This work attempts to develop a simple method to analyse the soil-pile pressure per unit length of the pile. The model is based on the theory of plastic deformation and is modified by considering both the inclination of the sliding ground and the soil arching effects along the depth of the sliding soil between two neighbouring piles. Comparisons have been made previously between the predicted results and the data from literature, as well as the results from Ito and Matsui [14]. The proposed model performs better than that of Ito and Matsui when predicting the soil-pile pressure per unit length of the pile in the slope. However, the prediction using the proposed method shows limited accuracy. Fig. 9, Fig. 11 and Fig. 12 still show some differences between the predictions and the numerical and experimental results. The assumption of neglecting the deformation of the piles during the movement of the soil is thought to result in the limited prediction. Furthermore, because the "squeezing effects" between two neighbouring piles are adopted from the theory of plastic deformation, the limitation of this theory is inherited as well [24,17]. The comparison mentioned above indicates that the proposed model is able to describe the distribution of the soil-pile pressure varying with the slope angle and that the trends of the soil-pile pressure are consistent with the literature data, but some differences in the values exist. To improve the prediction results, the model needs further modification in the future.

### 8. Conclusion

In this paper, the interaction between stabilizing piles and granular soil is analysed in a semi-infinite inclined sandy slope. A new theoretical model is proposed to evaluate the soil-pile pressure on stabilizing piles in a sandy slope based on the assumption that the soil displacement exceeds the pile deflection. In the proposed model, the soil arching zone is analysed using stress geometry. The soil arching effects are then considered to estimate the lateral active stress between two piles. Furthermore, the squeezing effects [14] between two neighbouring piles due to the deformation of the surrounding soils are adopted. To evaluate the proposed model, numerical simulations are implemented by FLAC<sup>3D</sup>. Comparing the predicted results from the proposed model, Ito and Matsui's approach and the simulations results reveals that Ito and Matsui's approach provides a linear solution for estimating the soil-pile pressure, while a nonlinear solution is obtained from the proposed model, which shows better agreement with the simulation results. In addition, the limited accuracy of the proposed model is also evaluated through comparison to the experimental data from the published literature.

A parametric analysis is also carried out on the slope angle and the internal friction angle. Both the slope angle and internal friction angle affect the distribution of the soil-pile pressure per unit length of the pile; the shape of the distribution of the soil-pile pressure is mainly affected by the slope angle, whereas the internal

friction angle has a greater effect on the magnitude of the soil–pile pressure on the pile than the slope angle. Additionally, the height of the resultant lateral force varies with the slope angle and the internal friction angle in the proposed model, whereas it remains constant in Ito and Matsui’s approach.

**Acknowledgment**

The authors extend their gratitude to editor-in-chief Scott. W. Sloan and two nominated reviewers for their insightful comments.

**Appendix A. Analysis of the geometric relationship in the soil arching zone**

When the soil stress on the line AB (Fig. 5) is active, the differential element (Fig. A1) and the corresponding Mohr’s circle (Fig. A2) are used to determine the geometric relationship between the stresses. The process of solving the angle  $\theta$  is as follows.

- (a) In a rectangular coordinate system, because the internal friction angle  $\varphi$  was investigated in advance, the strength envelope is determined as the line OP shown in Fig. A2.
- (b) The two lines OL and OL’ are drawn above and below the  $\sigma$  axis; the angle between each line and the  $\sigma$  axis is  $\beta$ .
- (c) On the line OL, we set  $OA = \sigma_z = \gamma z \cos \beta$ . Point A in Fig. A2 represents the stress acting on the surface (Fig. A1(b)), including the normal stress and the shear stress.
- (d) In the negative direction of the  $\sigma$  axis, an arbitrary point D’ is set. A circle can then be drawn with centre D’ and with tangency point B’ on the line OP’. The circle D’ and the line OE intersect at point A’.

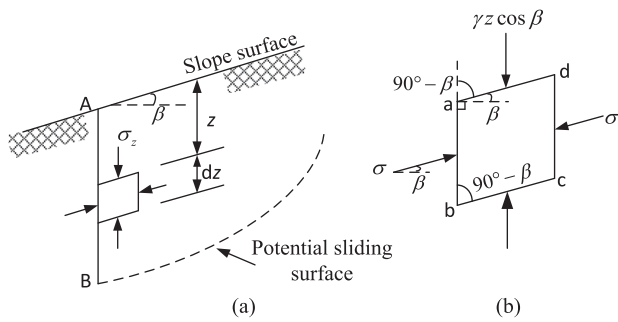


Fig. A1. The stress state: (a) the stress state of a differential element in a semi-finite slope; (b) the generic element.

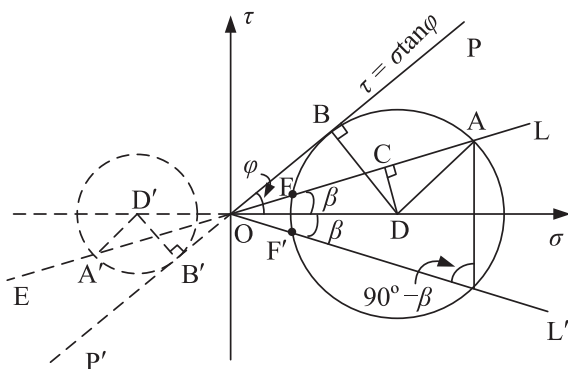


Fig. A2. The geometric relationship in the soil arching zone illustrated by Mohr’s circle.

- (e) Parallel to A’D’, a line AD is drawn with the point D located on the  $\sigma$  axis. Taking AD as the radius and point E as the centre, a circle is drawn. This produces the circle D, which is tangential to the line OP at point B.
- (f) The angle between AD and BD is equal to  $2\theta$ .

According to the geometric relationships in Fig. A2, it is obvious that

$$CD = OD \sin \beta \tag{A.1}$$

$$AD = BD = OD \sin \varphi \tag{A.2}$$

$$\cos \angle ADC = \frac{CD}{AD} = \frac{OD \sin \beta}{OD \sin \varphi} = \frac{\sin \beta}{\sin \varphi} \tag{A.3}$$

$$\angle ADC = \arccos \frac{\sin \beta}{\sin \varphi} \tag{A.4}$$

$$\theta = \frac{1}{2} \left( \varphi - \beta + \arccos \frac{\sin \beta}{\sin \varphi} \right) \tag{A.5}$$

$$\theta_1 = \frac{1}{2} \left( \varphi + \beta + \arccos \frac{\sin \beta}{\sin \varphi} \right) \tag{A.6}$$

**Appendix B. The squeezing effects between two neighbouring piles (Derivation of Eq. (24))**

The squeezing effects have been proven by Ito and Matsui [14] and are summarized as follows.

First, all of the assumptions that they made are adopted in this paper. In the zone EBB’E’ (Fig. 4), the equilibrium of the forces in the x direction on a differential element is considered (as shown in Fig. A3):

$$2dx \left[ \sigma_x \tan \left( \frac{\pi}{4} + \frac{\varphi}{2} \right) + \sigma_x \tan \varphi + c \right] - Dd\sigma_x - \sigma_x dD = 0 \tag{A.7}$$

The normal stress  $\sigma_x$  on the surface EBB’E’ (Fig. 4) is assumed to be equal to the principal stress  $\sigma_x$ . The Mohr–Coulomb’s yield criterion is expressed as:

$$\sigma_x = \sigma_x N + 2cN^{1/2} \tag{A.8}$$

in which  $N = \tan^2(\pi/4 + \varphi/2)$ . The geometrical condition gives:

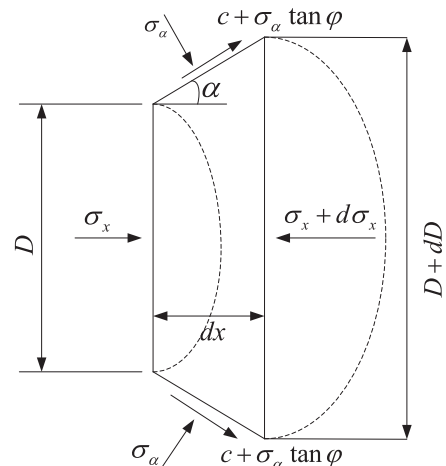


Fig. A3. Differential element (EBB’E’) between two neighbouring piles [14].

$$dx = \frac{d(D/2)}{\tan(\pi/4 + \varphi/2)} \tag{A.9}$$

Substituting Eqs. (A.8) and (A.9) into Eq. (A.7) and then integrating gives

$$\sigma_x = \frac{(C_1 D)^{(N^{1/2} \tan \varphi + N - 1)} - c(2 \tan \varphi + 2N^{1/2} + N^{-1/2})}{N^{1/2} \tan \varphi + N - 1} \tag{A.10}$$

where  $C_1$  is an integration constant.

Then, in the zone AEE'A' (Fig. 4), the equilibrium of the forces on a small soil element in the  $x$  direction is also considered, as shown in Fig. A4.

$$D_2 d\sigma_x = 2(\sigma_x \tan \varphi + c) dx \tag{A.11}$$

Substituting Eq. (A.8) into Eq. (A.11) and integrating gives

$$\sigma_x = \frac{C_2 \exp\left(\frac{2N \tan \varphi x}{D_2}\right) - c(2N^{1/2} \tan \varphi + 1)}{N \tan \varphi} \tag{A.12}$$

where  $C_2$  is an integration constant.

For sandy soil, the active earth pressure acts on the plane AA' (Fig. 4) and is obtained by Eq. (23), namely:

$$[\sigma_x]_{x=0} = \sigma_h = \frac{\gamma H K_{an}}{1 - K_{an} \tan \varphi \tan \beta} \left[ \left(1 - \frac{z}{H}\right)^{K_{an} \tan \varphi \tan \beta} - \left(1 - \frac{z}{H}\right) \right] \tag{A.13}$$

Eq. (A.13) is considered to be the boundary condition of Eq. (A.12); then,

$$C_2 = \sigma_h N \tan \varphi \tag{A.14}$$

Substituting Eq. (A.14) into Eq. (A.12) yields

$$[\sigma_x]_{x=\frac{D_1 - D_2}{2} \tan\left(\frac{\pi}{8} + \frac{\varphi}{4}\right)} = (\sigma_h N \tan \varphi) \exp\left[\frac{D_1 - D_2}{D_2} \cdot N \tan \varphi \tan\left(\frac{\pi}{8} + \frac{\varphi}{4}\right)\right] \tag{A.15}$$

The constant  $C_1$  in Eq. (A.10) is obtained by considering Eq. (A.15) to be the boundary condition. Then,

$$(C_1 D_2)^{(N^{1/2} \tan \varphi + N - 1)} = \frac{(N^{1/2} \tan \varphi + N - 1)}{N \tan \varphi} \times \left[ \sigma_h N \tan \varphi \cdot \exp\left(\frac{D_1 - D_2}{D_2} N \tan \varphi \tan\left(\frac{\pi}{8} + \frac{\varphi}{4}\right)\right) \right] \tag{A.16}$$

Eqs. (A.10) and (A.16) are used to obtain the solution of the lateral force  $P_{BB'}$  acting on the plane BB' (Fig. 4) per unit thickness of layer in the  $x$  direction, which is shown as follows:

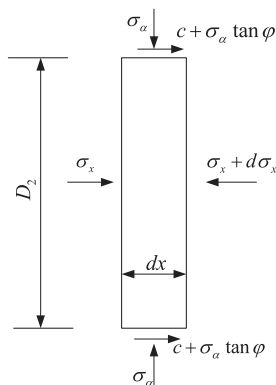


Fig. A4. Differential element (AEE'A') between two neighbouring piles [14].

$$P_{BB'} = D_1 \left(\frac{D_1}{D_2}\right)^{(N^{1/2} \tan \varphi + N - 1)} \left[ \sigma_h \cdot \exp\left(\frac{D_1 - D_2}{D_2} N \tan \varphi \tan\left(\frac{\pi}{8} + \frac{\varphi}{4}\right)\right) \right] \tag{A.17}$$

Finally, subtracting the active lateral force acting on the plane AA' from  $P_{BB'}$ , the soil–pile pressure per unit length of a pile in the  $x$  direction is obtained:

$$p = \frac{\gamma H K_{an} \cos \beta}{1 - (K_{an} \tan \varphi - K_{an} \tan \beta + m) \frac{\sin \theta}{\cos \theta_1}} \times \left[ \left(1 - \frac{z}{H}\right)^{(K_{an} \tan \varphi - K_{an} \tan \beta + m) \frac{\sin \theta}{\cos \theta_1}} - \left(1 - \frac{z}{H}\right) \right] \times \left\{ D_1 \left(\frac{D_1}{D_2}\right)^{N^{1/2} \tan \varphi + N - 1} \times \exp\left[\frac{D_1 - D_2}{D_2} N \tan \varphi \tan\left(\frac{\pi}{8} + \frac{\varphi}{4}\right)\right] - D_2 \right\} \tag{A.18}$$

Eq. (A.18) is the solution for the soil–pile pressure per unit length of a pile.

### Appendix C. Total lateral force and the point application of the force

The total lateral force  $p_t$  on a pile can be obtained by integrating Eq. (24) with respect to  $z$ :

$$p_t = \int_0^H p dz \tag{A.19}$$

Substitution of Eq. (24) into the above equation yields

$$p_t = \frac{\gamma H^2 K_{an} \cos \beta}{2 \left[ (K_{an} \tan \varphi - K_{an} \tan \beta + m) \frac{\sin \theta}{\cos \theta_1} + 1 \right]} \times \left\{ D_1 \left(\frac{D_1}{D_2}\right)^{N^{1/2} \tan \varphi + N - 1} \times \exp\left[\frac{D_1 - D_2}{D_2} N \tan \varphi \tan\left(\frac{\pi}{8} + \frac{\varphi}{4}\right)\right] - D_2 \right\} \tag{A.20}$$

The height of the point application of the force is obtained by dividing the moment of the soil–pile pressure about the failure surface by the total lateral force on a pile. The moment  $M$  of the soil–pile pressure about the failure surface is obtained as follow:

$$M = \int_0^H p(H - z) dz \tag{A.21}$$

Dividing Eq. (A.21) by Eq. (A.20) yields the height of the point application of the force,  $h_p$ :

$$h_p = \frac{\int_0^H p(H - z) dz}{p_t} = \frac{2 \left[ (K_{an} \tan \varphi - K_{an} \tan \beta + m) \frac{\sin \theta}{\cos \theta_1} + 1 \right]}{3 \left[ (K_{an} \tan \varphi - K_{an} \tan \beta + m) \frac{\sin \theta}{\cos \theta_1} + 2 \right]} \tag{A.22}$$

### References

- [1] Ashour M, Norris G, Pilling P. Lateral loading of a pile in layered soil using the strain wedge model. *J Geotech Geoenviron Eng ASCE* 1998;124(4):303–15.
- [2] Ashour M, Norris G. Modeling lateral soil–pile response based on soil–pile interaction. *J Geotech Geoenviron Eng ASCE* 2000;126(5):420–8.
- [3] Ashour M, Pilling P, Norris G. Lateral behavior of pile groups in layered soils. *J Geotech Geoenviron Eng ASCE* 2004;130(6):580–92.
- [4] Ashour M, Ardalan H. Analysis of pile stabilized slopes based on soil–pile interaction. *Comput Geotech* 2012;39:85–97.
- [5] Ausilio E, Conte E, Dente G. Stability analysis of slopes reinforced with piles. *Comput Geotech* 2001;28(8):591–611.
- [6] Chen LT, Poulos HG, Hull TS. Model tests on pile groups subjected to lateral soil movement. *Soils Found* 1997;37(1):1–12.

- [7] De Beer E. Piles subjected to static lateral loads. In: Proceedings of the 9th international conference on soil mechanics and foundation engineering, Special Session No. 10, Tokyo; 1977.
- [8] Durrani JK, Ellis EA, Reddish DJ. Modelling lateral pile–soil interaction for a row of piles in a frictional soil. In: 4th International FLAC symposium numerical modelling geomechanics; 2006. p. 231–8.
- [9] Griffiths DV, Lane PA. Slope stability analysis by finite elements. *Geotechnique* 1999;49(3):387–403.
- [10] Galli A, di Prisco C. Displacement-based design procedure for slope-stabilizing piles. *Can Geotech J* 2013;50(1):41–53.
- [11] Guo W, Ghee E. Behavior of axially loaded pile groups subjected to lateral soil movement. *Found Anal Des* 2006;174–81.
- [12] Hassiotis S, Chameau JL, Gunaratne M. Design method for stabilization of slopes with piles. *J Geotech Geoenviron Eng* 1997;123(4):314–23.
- [13] Kourkoulis R, Gelagoti F, Anastasopoulos I, Gazetas G. Slope stabilizing piles and pile-groups: parametric study and design insights. *J Geotech Geoenviron Eng ASCE* 2011;137(7):663–77.
- [14] Ito T, Matsui T. Methods to estimate lateral force acting on stabilizing piles. *Soils Found* 1975;21:21–37.
- [15] Ito T, Matsui T, Hong WP. Design method for stabilizing piles against landslide one row of piles. *Soils Found* 1981;21(1):21–37.
- [16] Ito T, Matsui T, Hong WP. Extended design method for multi-row stabilizing piles against landslide. *Soils Found* 1982;22(1):1–13.
- [17] Lee CY, Hull TS, Poulos HG. Simplified pile-slope stability analysis. *Comput Geotech* 1995;17(1):1–16.
- [18] Li XP, He SM, Wu Y. Seismic displacement of slopes reinforced with piles. *J Geotech Geoenviron Eng* 2010;136:880–4.
- [19] Liang R, Zeng SP. Numerical study of soil arching mechanism in drilled shafts for slopes stabilization. *Soils Found* 2002;42(2):83–92.
- [20] Lirer S. Landslide stabilizing piles: experimental evidences and numerical interpretation. *Eng Geol* 2012;149–150:70–7.
- [21] Martin GR, Chen CY. Response of piles due to lateral slope movement. *Comput Struct* 2005;83:588–98.
- [22] Norris G. Theoretically based BEF laterally loaded pile analysis. In: Proceedings of third international conference on numerical methods in offshore piling. Nantes, France; 1986. P. 361–86.
- [23] Paik KH, Salgado R. Estimation of active earth pressure against rigid retaining walls considering arching effects. *Geotechnique* 2003;53(7):643–53.
- [24] Poulos HG. Design of reinforcing piles to increase slope stability. *Can Geotech J* 1995;32:808–18.
- [25] Ugai K, Leshchinsky D. Three-dimensional limit equilibrium and finite element analysis: a comparison of results. *Soils Found* 1995;35(4):1–7.
- [26] Viggiani, C. Ultimate lateral loads on piles used to stabilized landslides. In: Proceedings of 10th international conference on soil mechanics and foundation engineers. vol. 3 Stockholm; 1981 p. 555–60.
- [27] Wang WL, Yen BC. Soil arching in slopes. *J Geotech Geoenviron Eng ASCE* 1974;61–79.
- [28] Wei WB, Cheng YM. Strength reduction analysis for slope reinforced with one row of piles. *Comput Geotech* 2009;36:1176–85.
- [29] Won J, You K, Jeong S, Kim S. Coupled effects in stability analysis of pile-slope systems. *Comput Geotech* 2005;32(4):304–15.
- [30] Zienkiewicz OC, Humpheson C, Lewis RW. Associated and non-associated visco-plasticity and plasticity in soil mechanics. *Geotechnique* 1975;25(4):671–89.